Environmental Science Advances

ROYAL SOCIETY OF CHEMISTRY

PAPER

View Article Online
View Journal | View Issue



Cite this: *Environ. Sci.: Adv.*, 2023, **2**, 967

# Electrospun $TiO_2$/carbon composite nanofibers as effective (photo)electrodes for removal and transformation of recalcitrant water contaminants†

Ashley Hesterberg Butzlaff,[a] Madeline Jensen,[a] Chenxu Yan,[b] Abdulsattar Ghanim,[c] Charles Werth,[b] David Cwiertny *[a] and Syed Mubeen *[c]

Electrochemical (EC) and photoelectrochemical (PEC) water treatment systems are gaining popularity, necessitating new electrode materials that offer reliable performance across diverse application platforms. For applications specifically targeting dilute chemical pollutants (*i.e.*, parts-per-million concentrations or less), beneficial electrode properties include high surface area to overcome kinetic overpotential losses, low electrode areal electrical resistance, and high water permeability with sufficient mechanical strength for use in electroactive membrane-based treatment systems. Here, we used electrospinning to fabricate (photo)electrodes from carbon nanofibers (CNFs) containing titanium dioxide ($TiO_2$) nanoparticles. Optimal CNF/$TiO_2$ composites were electrochemically and photochemically active with a surface area of ~50 $m^2$ $g^{-1}$ and electrode areal resistance of 2.66 Ω $cm^2$, values comparable to commercial carbon-based electrode materials (*e.g.*, Kynol Activated Carbon Cloth). Transformation experiments with carbamazepine (CBZ), a recalcitrant organic contaminant, suggest CNF/$TiO_2$ electrodes function dually as sorbents, first binding CBZ prior to oxidation at positive applied potentials. Complete CBZ transformation was observed in both EC (dark) and PEC (UV light; 280 mW $cm^{-2}$) systems over 90 minutes, with PEC systems exhibiting 1.5-fold higher transformation rates ($k_{obs}$ ~ 0.18 $min^{-1}$) at +1.00 V (*vs.* Ag/AgCl). Composite electrodes also exhibited stability across repeated use, yielding consistent current densities over five experimental cycles (120 min each) of CBZ transformation (0.25 ± 0.03 mA $cm^{-2}$). Because of their high surface area, electrical conductivity, photoactivity, and electrochemical stability, these electrospun CNF/$TiO_2$ composites represent promising (photo)electrode alternatives for diverse EC and PEC applications.

Received 24th January 2023
Accepted 3rd May 2023

DOI: 10.1039/d3va00017f

rsc.li/esadvances



## Environmental significance

An increasing number of emerging contaminants are present in drinking water supplies, and their risks to human health remain poorly understood. These unregulated contaminants provide unique challenges to traditional water treatment and affect many consumers, including those supplied by private wells. Electrochemical (EC) water treatment holds promise for addressing these challenges, using renewable energy to drive pollutant degradation with minimal chemical input in a decentralized platform. However, high-performance electrode materials remain a critical need for optimal performance, sustainability, and economic feasibility. To meet this need, we herein fabricate a carbon-based, nanoengineered composite electrode material for use in (photo)electrochemical water treatment and demonstrate its performance toward a persistent emerging organic contaminant common to drinking water supplies.

## Introduction

With the growing demand for technologies that can be driven by renewable energy sources, electrochemical (EC) and photoelectrochemical (PEC) systems have the potential to revolutionize water treatment.[1–4] EC treatment systems rely on the direct or indirect transfer of electrons between the dissolved pollutant target and the electrode surface under an applied potential.[3,5] Building upon EC systems, PEC systems integrate photochemistry to catalyze electrochemical reactions with light energy.[6,7] Unlike traditional photocatalytic (PC) systems (Fig. S1a†), PEC systems (Fig. S1b†) provide close contact between the semiconductor and a charge-collecting substrate to promote efficient carrier separation and transport as enabled by an external bias.[8–12] Further, by careful choice of (photo)cathode and (photo)anode materials, the entire reaction can be driven

[a]*Department of Civil and Environmental Engineering, University of Iowa, Iowa 52242, USA. E-mail: david-cwiertny@uiowa.edu*

[b]*Department of Civil, Architectural, and Environmental Engineering, The University of Texas at Austin, 301 E. Dean Keeton St, Stop C1786, Austin, Texas 78712-1173, USA*

[c]*Department of Chemical and Biochemical Engineering, University of Iowa, Iowa 52242, USA. E-mail: syed-mubeen@uiowa.edu*

† Electronic supplementary information (ESI) available. See DOI: https://doi.org/10.1039/d3va00017f

using renewable energy with improved efficiencies over a single-semiconductor PC system.[10,11,13]

The working electrode material is perhaps most critical to the performance of EC and PEC treatment systems. In addition to being environmentally (*e.g.*, nontoxic components) and economically responsible, electrode materials must also possess high surface area, electronic conductivity, stability during use, and water/gas permeability to satisfy diverse application platforms and the demand for improved performance over commercial available alternatives.[1–3] While PEC electrode materials have been extensively researched for hydrogen and oxygen production, fewer studies have explored suitable electrode materials for water treatment of dissolved chemical contaminants.[12,14–18] Indeed, a key practical challenge to implementing EC and PEC configurations in environmental systems is the low pollutant concentrations – typically ranging from parts per trillion (ng $L^{-1}$) to parts per million (mg $L^{-1}$) – that induce large kinetic losses at the electrode surface due to mass transport overpotentials. To overcome this and other challenges, work to date has established several favorable electrode properties for EC and PEC water treatment applications including: (i) large interfacial contact between the semiconductor and aqueous phase to decrease kinetic overpotential losses and to maximize light absorption;[19–21] (ii) improved carrier collection to minimize recombination;[22,23] and (iii) high material strength for durable operation.[22–24] Moreover, water permeability is desired to overcome mass transfer limitations, particularly for electrodes acting as reactive (*i.e.*, electroactive) membranes in dead-end or cross-flow filtration systems.[25,26]

To date, common electrode materials include noble metals, metal oxides (*e.g.*, tungsten, titanium, bismuth, iron) and mixed metal oxides (MMO), graphite, and boron-doped diamond (BDD) electrodes.[21,27–29] Integrating a co-catalyst or photocatalyst in these materials can expand applications to PEC systems.[29–32] More recent efforts have focused on further developing engineered nanomaterials for use in EC and PEC systems to take advantage of the large surface area to volume ratios, enhanced mass transfer, and improved control of electron flow (*i.e.*, product selectivity).[3,32,33] In particular, carbon nanofibers (CNFs) have become a popular choice for self-supported electrodes because the desirable properties of carbon [*e.g.*, (electro)chemical stability, electrocatalytic activity, wide potential window, low cost][22,34] are enhanced in a nanostructured, three-dimensional fiber network that provides improved surface area, pore structure, electrical conductivity, and mechanical flexibility.[35,36] Moreover, CNF composites that include secondary components (*e.g.*, a nanoparticle semiconductor) can also be fabricated to introduce properties not realized in carbon-only materials (*e.g.*, photoactivity).[28] Although some studies with composite CNF electrodes have demonstrated efficient transformation of environmental pollutants in EC and PEC systems, many prior studies have focused on pollutant targets of limited relevance to emerging water treatment needs (*e.g.*, targeting dyes at high concentrations),[28] have been fabricated using toxic materials not suitable for water treatment,[27] or employ electrodes and catalysts that may be cost prohibitive (*e.g.* BDD, platinum group metals).[2,3,37]

Herein, we fabricated, characterized, and assessed the performance of electrospun CNFs containing titanium dioxide ($TiO_2$) nanoparticles for use as both an electrode and a photoelectrode (in the presence of light) for pollutant transformation. Results from this work demonstrate the potential advantages of the proposed (photo)electrode architecture and design while avoiding complex systems or components (*e.g.*, catalyst recovery, catalyst leaching, additional chemical and energy inputs).[38–40] The electrospun CNFs serve as a three-dimensional, low-resistance current collector and provide a high surface area for supporting and exposing embedded $TiO_2$ semiconductor particles for enhanced charge transport. $TiO_2$ – an earth-abundant semiconductor that represents the industry standard for photocatalytic water treatment applications[41,42] – was selected due to the extensive literature about its performance as a photocatalyst, particularly for pollutant transformation.[14,43–49] While the work builds upon our prior study that utilized CNF/$TiO_2$ composites as a photocatalytic membrane for treating organic micropollutants,[47] we herein show for the first time that by carefully controlling synthesis parameters, these materials can also function as both electroactive and photoelectroactive substrates for transforming pollutants recalcitrant to photocatalytic approaches alone.

Using electrospinning, an industrially viable route to large-scale nanofiber fabrication,[50] we produced a suite of CNF/$TiO_2$ composites with varying $TiO_2$ levels (30–70 wt% relative to polymer mass) and thicknesses (from 170–520 μm). Through electrochemical characterization using potentiostatic electrochemical impedance spectroscopy (PEIS), we demonstrate that the optimal CNF/$TiO_2$ (photo)electrodes can achieve geometric (areal) resistances ($\Omega\ cm^2$) comparable to commercial activated carbon electrodes (Kynol Activated Carbon Cloth 5092-10; Gun EI Chemical Industry Japan) while demonstrating higher ion mobility by two orders of magnitude ($D = 2.70 \times 10^{-8}\ cm^2\ s^{-1}$). We then evaluated the performance of the CNF/$TiO_2$ composites as electrodes and photoelectrodes in batch water treatment systems targeting the organic micropollutant carbamazepine (CBZ), which is recalcitrant to traditional water treatment approaches.[51] The CNF/$TiO_2$ (photo)electrodes demonstrated rates for CBZ transformation that compared favorably to those reported for PC treatment with $TiO_2$ suspensions.[52,53] The (photo)electrodes also provided consistent EC performance over multiple reaction cycles with CBZ.

## Materials and methods

### Reagents

All reagents are listed in the ESI.†

### Electrode synthesis

**Electrospinning.** Following our previous work,[47] electrospun CNF electrodes were produced from sol-gels of polyacrylonitrile (PAN) dissolved in *N*,*N*-dimethylformamide (DMF). Sol–gels also included a predetermined weight percentage (from 30 to 70 wt% relative to PAN) of $TiO_2$ nanoparticles (Evonik P25; approximately 75% anatase/25% rutile, mean diameter 21 nm,

specific surface area 50 $m^2 g^{-1}$) and phthalic acid (PTA; 2.5 wt% relative to total sol–gel mass) to improve suspension stability and to provide fiber porosity.[47,54]

To prepare the sol–gels, first, $TiO_2$ and PTA were uniformly dispersed in DMF by ultrasonication for five hours. After sonication, PAN was added to the $TiO_2$ with PTA suspension and thermomixed (2 hours, 60 °C, 700 rpm) to produce a homogeneous sol–gel with no visible settling. All sol–gels were prepared with a PAN concentration of 8 wt% relative to total sol–gel mass (*i.e.*, PAN + DMF + PTA).

To vary the thickness of deposited nonwoven nanofiber mats, the sol–gel volume used during electrospinning was increased. For these materials, sol–gel components were scaled by a factor of 0.5, 1.0, or 1.5 (corresponding to sol–gel DMF volumes of 1.75, 3.5, and 5.25 mL, respectively), where the relative weight percent of each component within the sol–gel was held constant (*e.g.*, PAN concentration of 8 wt% was held constant with volume). Because the electrospun nanofibers were collected on a rotating, grounded collector of constant surface area, CNF mat thickness could be expected to increase with increasing sol–gel volume.

Fig. S2† shows all the different electrospinning solution formulations used in this study. Hereafter, each material will be identified as "XX g PAN/XX wt% $TiO_2$" to specify the $TiO_2$ composition and polymer mass, respectively, as determined by the sol–gel composition. A lab-scale, custom-designed rig described in our earlier work was used for electrospinning.[54] The detailed electrospinning procedure and parameters are provided in the ESI.† A photograph of the electrospinning rig is shown in Fig. S3.†

**Stabilization and carbonization.** Following electrospinning, composites were sequentially stabilized under air (to cross-link polymer chains) and carbonized under nitrogen (to expunge non-carbon elements).[55–59] Thermal oxidative stabilization in the air occurred at 250 °C for 2.5 hours (5 °C $min^{-1}$ ramp). Once stabilized, the material was carbonized under nitrogen gas at 450 °C for 1 hour (5 °C $min^{-1}$ ramp) in a tube furnace (OTF-1200X, MTI Corporation). Carbonization temperature was varied (450, 575, 750, or 1000 °C) to determine structural and performance trends with temperature. Fig. S4† shows a digital photograph of sequential changes to the electrospun mats after each fabrication step. Samples were weighed before each process to determine the mass lost during each heat treatment step. Composite materials fabricated at various carbonization temperatures will hereafter be identified as "XX g PAN/XX wt% $TiO_2$/XX °C".

## Nanofiber characterization

**Physical properties.** To evaluate CNF surface morphology, scanning electron microscopy (SEM; Hitachi S-4800 FE-SEM) images were collected, and fiber diameter and mat thickness were measured (ImageJ, NIH). Fiber diameters for each composite formulation were reported as histograms ($n = 85$). To verify that our synthesis provided reproducible fiber diameter distributions, outliers were determined with respect to the interquartile range (IQR) and the lower (Q1, 25th percentile) and upper (Q3, 75th percentile) quartiles (Q1 − 1.5 × IQR; Q3 + 1.5 × IQR). Mat thickness was obtained *via* cross-sectional imaging, where samples were placed between two paperboard supports and secured perpendicular to pin stubs with conductive carbon tape. For each prepared sample, multiple measurements were recorded along the sample length ($n = 22$), and thickness was reported as an average value of those measurements. All SEM samples were sputter-coated with a thin gold layer prior to imaging.

Energy-dispersive X-ray spectroscopy (EDS) was performed in tangent with SEM (IXRF Systems; 15 kV) to provide the elemental mapping of the optimal fiber composite. Transmission electron microscopy (TEM; Hitachi HT7800) images were also collected for the optimal fiber composite to examine the internal fiber structure and distribution of $TiO_2$ nanoparticles within the fibers. For TEM analysis, samples were suspended in acetonitrile overnight and drop-cast onto carbon-coated TEM grids.

Specific surface area ($S_{BET}$) and pore volume measurements were conducted under nitrogen using a surface area and pore size analyzer (Quantachrome Nova 4200e). Methods to quantify specific surface area and pore volume are provided in the ESI.† $TiO_2$ crystal structure (anatase, rutile) as a function of carbonization temperature was identified by powder X-ray diffraction (XRD; Bruker D-5000 q – q diffractometer). Similarly, the graphitic character of CNFs fabricated at different carbonization temperatures was identified with Raman spectroscopy (Renishaw), which indicates the extent of graphitic molecular structures using the relative D-band (~1350 $cm^{-1}$) and G-band (~1580 $cm^{-1}$) intensities.[60,61]

Bulk (macroscale) tensile strength (Young's modulus, kg $mm^{-2}$) was measured with a universal test machine equipped with grips and a 50 N load cell (Lloyds Instruments LF-Plus). For tensile testing, samples were cut into coupons with a dog-bone template (35 mm in length, 4 mm in width) and separated uniaxially at a constant rate of 3.5 mm $min^{-1}$, following the guidelines established in ASTM D882-18.[62]

**Electrochemical properties.** Electrochemical properties – including charge transfer resistance ($R_{ct}$), total resistance ($R_{tot}$), ohmic resistance ($R_{ohm} = R_{tot} - R_{ct}$), and mass transport resistance – for each composite were determined by potentiostatic electrochemical impedance spectroscopy (PEIS) (Biologic VSP-300 Potentiostat), with data fit using the Simple Randles circuit. The Simple Randles circuit model (Fig. S5†) was selected to ensure an accurate fit while providing conservative resistance and avoiding superfluous circuit elements. A custom-built Teflon microreactor was used for PEIS studies (Fig. S6†). All resistance values are reported with respect to the geometric area of the sample exposed to solution in the microreactor (0.5 $cm^2$). Table S1† summarizes the optimized PEIS experimental parameters used to collect the reported data.

Diffusive processes may govern the limiting current and kinetics in an electrochemical system by restricting ion transport to and from the electrode surface (*i.e.*, mass transfer effects). To quantify mass transfer effects for composite electrodes with different $TiO_2$ loadings and carbonization temperatures (450, 1000 °C), the diffusion coefficient ($D$) was

determined by a data-based method,[63] which utilizes information provided by PEIS data as represented by the Randles circuit. The details to and equations for this method are provided in the ESI.† In brief, real impedance ($Z'$) values from PEIS data in the low-frequency range (<10 Hz), where diffusive processes are relevant, were used to determine the Warburg coefficient ($\sigma_w$) (eqn (S3)–(S5)†). Once $\sigma_w$ was obtained, the diffusion coefficient was calculated (eqn (S6)†).

### Contaminant transformation experiments

Three different systems were examined for transformation studies: photochemical (PC), electrochemical (EC), and photoelectrochemical (PEC). Before all transformation experiments, staircase cyclic voltammetry (SCV) was conducted with CBZ to probe electron transfer processes and to examine the faradaic current available under experimental conditions. SCV was selected to eliminate any current contribution from capacitive (non-faradaic) behavior of the composites. SCV was obtained from −0.70 to +1.55 V *vs.* Ag/AgCl with a 50 mV step size every 30 seconds. This potential range was selected to capture the positive currents resulting from CBZ oxidation while maintaining reasonable operating conditions for EC and PEC systems.

Before the start of each contaminant transformation experiment, the CNF/$TiO_2$ composite ($SA_{geo} = 11.5\ cm^2$) was placed in 10 μM CBZ in 0.5 M phosphate buffer solution (PBS) at circumneutral pH overnight in the dark to reach sorption equilibrium with CBZ. The initial CBZ concentration for transformation experiments ($C_0$ = 10 μM) was greater than typical concentrations in environmental systems (μg $L^{-1}$ concentrations or less), but this initial concentration was selected to provide accurate analytical detection for a complete mass balance resulting from each experimental step (sorption, transformation, and extraction). After the end of this sorption period, a constant potential was applied (+0.25 to 1.00 V *vs.* Ag/AgCl) (Biologic VSP-300 Potentiostat) to composites used for EC and PEC experiments. For PEC experiments, the composite was exposed to UV/visible irradiation using a 1000 W xenon arc lamp (Newport Corporation) with a 225 nm cut-on filter (10CGA-225, Newport; 280 mW $cm^{-2}$) in addition to the constant applied potential. We note that for PEC and EC experiments at all applied potentials, the average geometric current density ($J_{geo}$) excluded the high capacitive current at potential onset (≤300 s). Finally, for PC transformation experiments, only UV/vis radiation (without a constant potential) was applied to the composite after the initial sorption period.

Aqueous samples were taken periodically over a 90 minute transformation period (700 μL per sample) to quantify the dissolved CBZ concentration *via* high-performance liquid chromatography (HPLC-DAD, Agilent 1100 Series). Additional HPLC method details are provided in the ESI.† At the end of the 90 minute transformation period, CNF/$TiO_2$ composites were removed from the batch system and placed in organic solvent (methanol or acetonitrile) for 24 hours to extract any CBZ remaining on the composite surface or within the fiber matrix. Both methanol and acetonitrile achieved near-complete recovery in controls. After 24 hours, the extraction solvent was sampled and analyzed *via* HPLC to determine the amount of CBZ mass that remained bound to the CNF/$TiO_2$ at the end of the 90 minute transformation period. This analytical approach provides a complete mass balance for CBZ in our system, from which the mass of CBZ transformed could be determined: (transformed mass) = (initial aqueous mass) − (final aqueous mass) − (sorbed mass).

As a measure of electrode reactivity toward CBZ, we also estimated the pseudo-first-order rate constant for CBZ transformation in EC and PEC systems. This was accomplished by assuming exponential decay of CBZ over the first 15 minutes of applied potential (+1.00 V *vs.* Ag/AgCl) with or without light. This shortened transformation period allowed for sufficient degradation of CBZ to reasonably estimate a reaction rate constant while also having sufficient CBZ mass remaining in solution and sorbed to the CNF/$TiO_2$ for reliable quantification.

The stability and sustained performance of the CNF/$TiO_2$ composite were also assessed across five reaction cycles with CBZ (*i.e.*, overnight sorption period followed by EC transformation at +1.00 V *vs.* Ag/AgCl for 120 minutes). After each transformation period, the solution was discarded, and a new solution volume ($C_0$ = 10 μM CBZ) was added to start the sorption period of the next cycle. After the final transformation period, the composite electrode was removed from solution and placed in organic solvent for 24 hours to extract any CBZ remaining on the electrode surface (as previously described for all other transformation experiments).

## Results and discussion

### Electrode properties

**Bulk structural properties across $TiO_2$ content.** Fig. 1 shows top-view and cross-sectional SEM images with corresponding histograms of nanofiber diameters for CNF/$TiO_2$ composite fiber diameters after carbonization at 450 °C.

The SEM images revealed that fiber diameter increased with the addition of $TiO_2$, increasing nearly three-fold from CNFs without $TiO_2$ (140 ± 20 nm) to CNFs with 70 wt% $TiO_2$ (410 ± 90 nm). This increase in diameter is likely due to changes in sol–gel properties in response to increasing $TiO_2$ loading; for example, sol–gel viscosity and conductivity are known to influence the diameter of fibers produced *via* electrospinning.[54,64,65]

We note that CNFs with 50 wt% $TiO_2$ exhibited the widest distribution in measured diameters, as evidenced by their considerably larger standard deviation (270 ± 140 nm). We attribute this to some regions along the 50 wt% CNF fibers retaining the diameter of pure CNFs while other areas had $TiO_2$ aggregates that increased diameter. Indeed, the presence of these aggregates was easily discerned in TEM images, shown in Fig. 2 for 0.45 g of PAN/50 wt% $TiO_2$ composite fibers. Despite the presence of these aggregates, SEM-EDS analysis suggests that $TiO_2$ is distributed throughout the fiber matrix (Fig. S7†), thus we do not expect the presence of these aggregates will adversely influence the (photo)electrochemical performance of these materials.

The specific surface area of the CNF/$TiO_2$ composites, as previously determined from $N_2$ adsorption–desorption

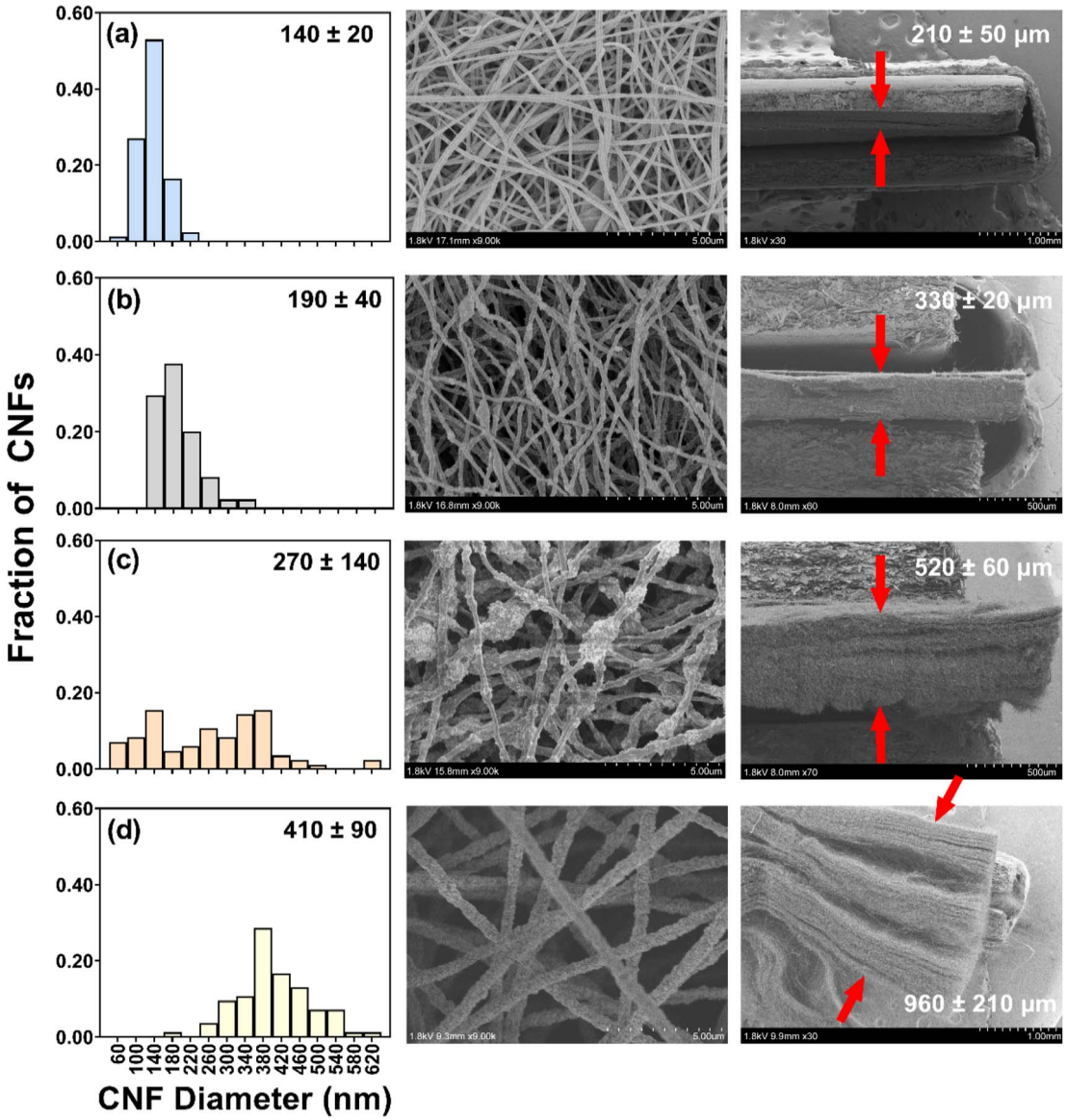


Fig. 1 SEM images of CNF/$TiO_2$ composites fabricated with 0.45 g PAN (corresponding to 1.5× sol–gel scaling) and carbonized at 450 °C as a function of $TiO_2$ wt%: (a) 0, (b) 30, (c) 50, and (d) 70. Values in histograms represent mean fiber diameter and standard deviation ($n = 85$). Values in cross-sectional images represent mean thickness and standard deviation ($n = 22$). Distance between arrows identifies the electrode thickness as measured.

isotherms,[47] increased with $TiO_2$ loading. Composites containing $TiO_2$ at 33, 50, and 80 wt% possessed specific surface areas of 13, 25, and 50 $m^2\ g^{-1}$, respectively. This is presumably due to the higher specific surface area of the embedded $TiO_2$ nanoparticles, which become more abundant on the composite surface at higher loadings.

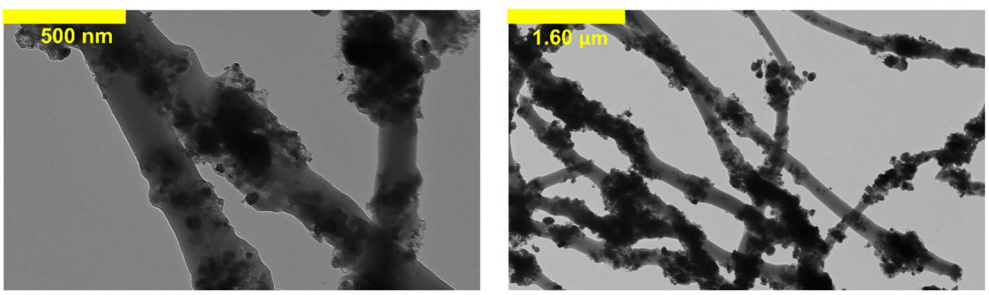


Fig. 2 TEM images of CNF/$TiO_2$ composites with 50 wt% $TiO_2$.

For CNF/$TiO_2$ composites electrospun with the same total sol–gel volume and PAN mass, cross-sectional SEM images revealed a notable increase in the mat thickness with increasing $TiO_2$ loading (210 ± 50 μm without $TiO_2$ to 520 ± 60 μm with 50 wt% $TiO_2$; approximately a 2.5-fold increase; see Fig. 1). This trend in mat thickness can primarily be attributed to the observed increase in individual fiber diameter with increasing $TiO_2$ content, which is expected to influence the packing density of nanofibers within the three-dimensional fiber network. It is also possible that the increasing content of $TiO_2$ introduces more electrostatic interactions between the hydroxylated oxide surfaces, resulting in some charge repulsion between fibers that also increases mat thickness. In fact, the nonwoven CNF mats exhibited less cohesiveness at the highest $TiO_2$ loading considered (70 wt%), where mats separated into distinct layers upon cross-sectioning, and henceforth were not prioritized for extensive electrochemical characterization.

For mats with the same $TiO_2$ content, the thickness of the deposited nanofiber layer also varied with the total sol–gel volume and PAN mass, as anticipated. Cross-sectional images are shown in Fig. S8† for composites with 50 wt% $TiO_2$ for sol–gels containing 0.15, 0.30, and 0.45 g of PAN (corresponding to 1.75, 3.75, and 5.25 mL DMF). Because the surface area of the grounded collector was the same in all cases, the thickness of the composite nanofiber layer increased with PAN mass from 170 (±30 μm) (thinnest) to 520 (±30 μm) (thickest).

**Bulk structural properties across carbonization temperature.** Bulk mass was recorded after electrospinning, stabilization, and carbonization, with mass progressively decreasing with each successive synthesis step (electrospinning, stabilization, carbonization). The mass remaining after carbonization at 1000 °C, which is primarily composed of carbon and $TiO_2$ as shown by XRD and Raman (discussed below), is between 50–65% of the initially deposited polymer composite. Mass lost during stabilization is attributed to dehydrogenation and cyclization reactions[66] while mass lost during carbonization is attributed to volatilization of nitrogen- and oxygen-containing components.[57,67] Further, composites also lost mass when PTA decomposed during heat treatment, which can begin at 196–199 °C.[68] Despite this mass loss, we found all composite CNFs, even those carbonized at 1000 °C, to be sufficiently durable such that they could be manipulated as (photo)electrodes in our experimental set-up. For example, Fig. S9† illustrates simple bending and rotational tests that support CNF/$TiO_2$ mat durability and stability, where this degree of handling would be sufficient for their use in many reactor designs. Moreover, the average fiber diameter for composites containing 50 wt% $TiO_2$ was comparable when carbonized at 450 and 1000 °C (see Fig. S10†). However, we observed an increase in the average thickness at 1000 °C compared to 450 °C (Fig. S10†). We attribute this increase in thickness at higher carbonization temperature to changed fiber characteristics (*e.g.*, more electrostatic repulsion between fibers) that produce less densely packed fibers.

As a more quantitative measure of material strength through the carbonization process, macroscale tensile strength testing for 0.45 g PAN/50 wt% $TiO_2$ carbonized at 1000 °C provided Young's modulus of 3.8 (±1.0) MPa. This modulus is within the range of values previously provided from a systematic investigation on the strength of nonwoven PAN-based carbon mats fabricated *via* electrospinning.[69] However, we note that this modulus does not exceed the tensile strength of some commercial carbon fibers.[70]

Surface area and pore size characterization of the synthesized 0.45 g PAN/50 wt% $TiO_2$ composites carbonized at 450 and 1000 °C was performed using adsorption–desorption $N_2$ isotherms (Fig. S11†). From 450 to 1000 °C, the surface area ($S_{BET}$) increased by 1.75-fold and total pore volume ($V_{tot}$) increased by 2.5-fold. Composites carbonized at 1000 °C exhibit greater cumulative pore volume and more pore volume at larger pore sizes. Fig. S12† exhibits a larger mesopore as observed *via* SEM for 0.45 g PAN/50 wt% $TiO_2$/1000 °C. A detailed discussion on the pore distribution and the corresponding values (see Table S2) are presented in the ESI.†

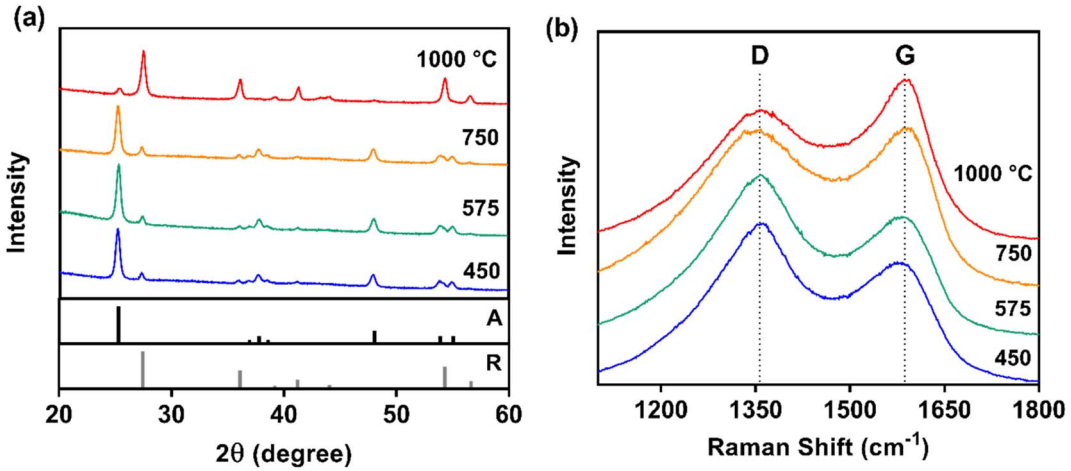


Fig. 3 (a) XRD patterns for 0.45 g PAN/50 wt% $TiO_2$ composites as a function of carbonization temperature, with reference diffraction patterns also shown for anatase (A) and rutile (R). (b) Corresponding Raman spectra for these composites, with the amorphous (D-band) and graphitic (G-band) carbon bands indicated by dashed vertical lines.

XRD confirmed that the anatase crystal structure of $TiO_2$ remained dominant at low carbonization temperatures (≤750 °C), and the rutile phase became dominant after carbonization at 1000 °C (26% anatase and 74% rutile) (Fig. 3a). Although the rutile crystal structure is known to have excellent electron transfer, the anatase crystal structure – which is thermodynamically unstable at higher temperatures – possesses greater photoactivity for applications in photocatalysis and photoelectrochemistry.[71] This crystal structure transition near 1000 °C also agrees with previous work demonstrating a similar shift for $TiO_2$ nanopowder processed sequentially under air and in vacuum at different temperatures.[72]

Because the XRD peaks corresponding to graphite ($2\theta = 26$, 43, and 53°) were overwhelmed by the peaks for $TiO_2$, Raman spectroscopy was used to examine the CNF carbon crystal structure (Fig. 3b), confirming a similar transition with temperature. Graphitic character ($R$-value) and in-plane crystalline size ($L_a$) increased with carbonization temperature (Table S3†). The $R$-value (graphitic character) increased most notably from 575 to 750 °C, where composites carbonized at 750 °C exhibited markedly different G-band and D-band signatures compared to lower temperatures. Increased G-band intensity indicated ordered (graphitic) carbon became the dominant phase for carbonization temperatures of 750 °C and above. At the highest carbonization temperature (1000 °C), composites had the greatest graphitic character ($R$-value = 0.81) and the largest in-plane crystalline size (0.54 nm). Graphitic materials with larger in-plane crystallite size are more desirable for electrochemical applications because they exhibit lower electrical resistance as it facilitates carrier hopping between crystallites.[61] This trend in carbon structure agrees with the prevailing theory that in-plane crystallite size can be controlled with heat treatment temperature and duration.[61]

**Electrochemical characterization.** Electrochemical characterization results from PEIS are summarized in Fig. 4. Modeling of the PEIS results using the Simple Randles circuit (see model in Fig. S5†) revealed that at high frequency, charge transfer resistance ($R_{ct}$) results from the electrode and electrolyte. At low frequency, $R_{ct}$ is attributed to the oxide component of $TiO_2$.

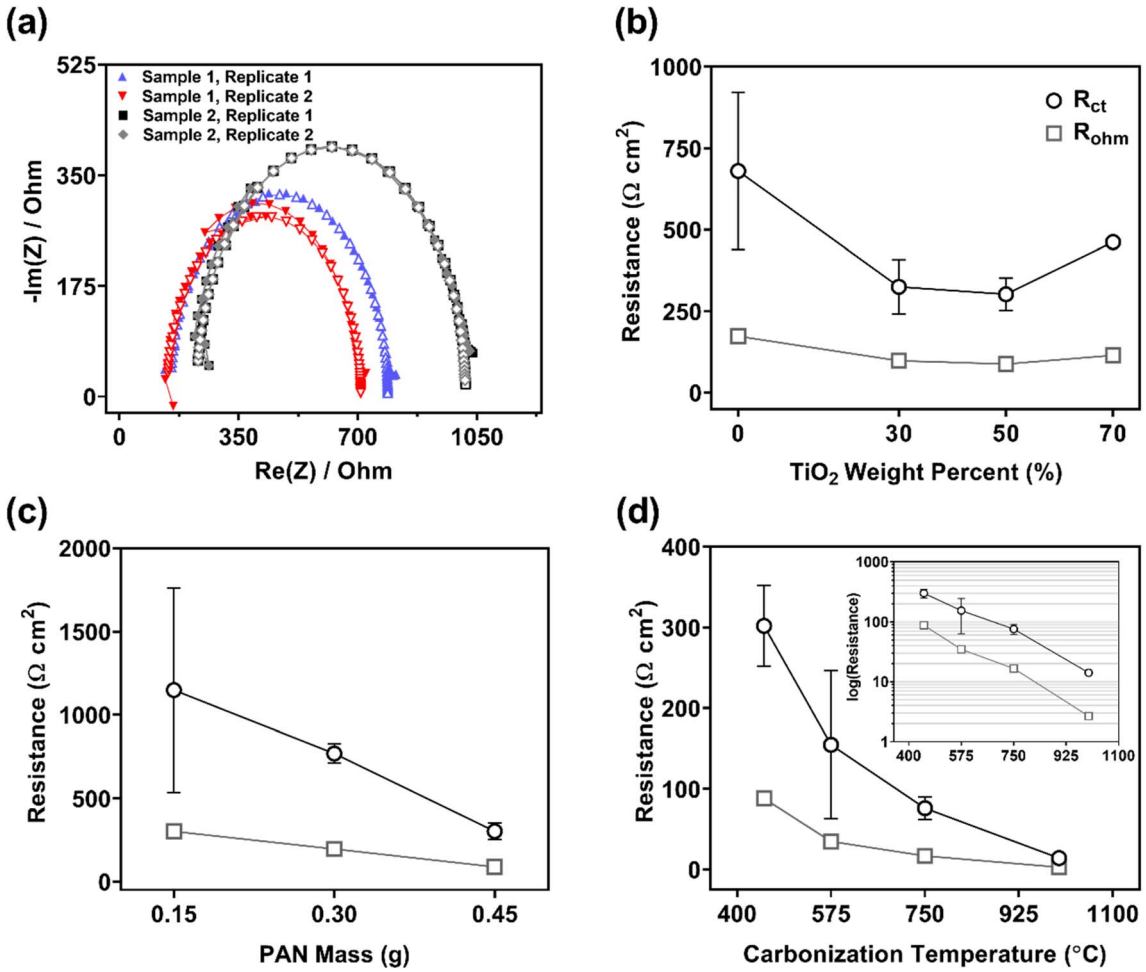


Fig. 4 (a) Typical Nyquist plots obtained from PEIS data (▲) for 0.45 g PAN/50 wt% $TiO_2$ composites and corresponding fit (△) by the Simple Randles circuit (see Fig. S5†). The data demonstrate consistency between replicates and batches. (b) Charge transfer resistance ($R_{ct}$) and ohmic resistance ($R_{ohm}$) for 0.45 g PAN/$TiO_2$ composites. Standard deviation for 70 wt% composite is small relative to scale. (c) $R_{ct}$ for 50 wt% $TiO_2$ composites with varying PAN mass (0.15, 0.30, and 0.45 g). (d) $R_{ct}$ and $R_{ohm}$ for 0.45 g PAN/50 wt% $TiO_2$ electrodes carbonized at 450, 575, 750, and 1000 °C. PEIS parameters are listed in the ESI.†

Using this approach, we found that areal resistance values (Ω $cm^2$) obtained from PEIS data were dependent upon the structure and composition of the electrode materials.

An important aspect of this work was demonstrating the reproducible synthesis of composites based on their electrochemical performance metrics. Accordingly, Fig. 4a shows PEIS results obtained for two sample materials of 0.45 g PAN/50 wt% $TiO_2$. Note, in all cases, samples were synthesized from different sol–gels prepared on different days. The agreement in data – across samples and between replicates (*i.e.*, using different sections from the same sample) – demonstrated the ability of our synthesis approach to consistently produce electrode materials with reproducible electrochemical performance. Indeed, in Table S4,† we report average $R_{ct}$ and $R_{tot}$ values (with standard deviations) from two replicates per sample from samples fabricated over a six-month period. Greater deviation for 0 wt% $TiO_2$ electrodes and for the thinnest electrodes is attributed to their lower material strength. These more fragile electrodes could not be reliably tested because they often broke.

**Resistance across $TiO_2$ content.** Fig. 4b shows how the measured resistance of different electrode materials changed with increasing $TiO_2$ content. CNFs without $TiO_2$ exhibited the greatest resistance while CNFs with $TiO_2$ generally demonstrated decreasing resistance with increasing $TiO_2$ content. Although carbon is regarded as a highly conductive material, we observed a decrease in resistance with increased $TiO_2$ content (a semiconductor) because: (i) surface area for CNFs with $TiO_2$ is greater than for carbon only CNFs (approximately 6-fold increase from 0 wt% to 50 wt% $TiO_2$),[47] and (ii) conductivity is measured with electrochemical impedance spectroscopy (EIS) to represent the electroactivity of the electrode, which plays an important role because carbon–$TiO_2$ composites have demonstrated improved electroactivity (*i.e.*, conductivity, ion diffusivity, capacitance) relative to pure carbon.[73–77]

We observed the lowest resistance for 30 and 50 wt% $TiO_2$ composites, with $R_{ct}$ = 330 (±80) and 300 (±50) Ω $cm^2$, respectively. Although composites with 30 and 50 wt% $TiO_2$ exhibited comparable areal resistance, 50 wt% $TiO_2$ composites were preferred over 30 wt% $TiO_2$ composites because they also exhibited less variability in performance between replicates and samples (based on standard deviation of reported performance metrics). Composites with 70 wt% $TiO_2$ demonstrated higher resistance ($R_{ct}$ = 460 ± 10 Ω $cm^2$) than 30 and 50 wt% $TiO_2$, which may be due to the lower structural integrity at this high $TiO_2$ loading (see cross-sectional images in Fig. 1). Ultimately, composites with 50 wt% $TiO_2$ were selected as the optimal composite CNF electrode and used for all subsequent analysis and experiments.

**Resistance across electrode thicknesses.** For composites with 50 wt% $TiO_2$, resistance decreased as the total amount of PAN mass (DMF volume) used in electrode fabrication (and thus the overall thickness of the final carbonized electrode) was increased (Fig. 4c). The smallest PAN mass (*i.e.*, thickness) provided $R_{ct}$ = 1150 (±600) Ω $cm^2$ while the largest PAN mass provided $R_{ct}$ = 300 (±50) Ω $cm^2$. This trend in resistance with increasing electrode thickness can be easily rationalized; increased thickness provides increased surface area for improved electron transfer due to a greater number of fibers and inter-fiber connectivity.

**Resistance across carbonization temperatures.** Fig. 4d shows resistance values for 0.45 g PAN/50 wt% $TiO_2$ composites fabricated at different carbonization temperatures. As anticipated, resistance decreased with increasing carbonization temperature due to the corresponding changes in carbon content and graphitic character (see Fig. 3b). A minimum resistance ($R_{ct}$ = 15 ± 0.5 Ω $cm^2$) was obtained for composites carbonized at 1000 °C due to increasing graphitic character (*R*-value = 0.81) and more conductive $TiO_2$ structure (26%A : 74% R). Although we anticipate that graphitic character may further develop at temperatures ≥1000 °C, this behavior was not investigated herein because composites are likely to become increasingly brittle and prone to breaking.

**Diffusion coefficients (*D*).** tThe diffusion coefficient (*D*) for each material was determined from real impedance values at low frequency (<10 Hz) following a data-based method (further discussed in the ESI†).[63] The diffusion coefficients, as derived from PEIS data, are presented in Table S5.† When carbonized at 450 °C, composites containing 30 and 70 wt% $TiO_2$ had similar coefficients ($D = 10^{-15}$ $cm^2$ $s^{-1}$) while composites with 50 wt% $TiO_2$ had the largest coefficient ($10^{-14}$ $cm^2$ $s^{-1}$). For composite electrodes with 50 wt% $TiO_2$, *D* values increased by several orders of magnitude with increasing carbonization temperature from 450 to 1000 °C ($10^{-8}$ $cm^2$ $s^{-1}$). This may be due to structural changes, as supported by $N_2$ adsorption analysis (*e.g.*, increased porosity), observed at higher carbonization temperatures. We note that our optimal 0.45 g PAN/50 wt% $TiO_2$/1000 °C composites exhibited less mass transfer resistance when compared to similar commercial electrode materials ($10^{-10}$ $cm^2$ $s^{-1}$; Kynol Activated Carbon Cloth 5092-10), which we measured using the same approach as that for our CNF/$TiO_2$ electrodes.

## Contaminant transformation

**Electrochemical transformation of CBZ on CNFs and CNF/$TiO_2$ composites.** Fig. 5 shows the change in aqueous carbamazepine (CBZ) concentration ($C_0$ = 10 μM) over time through the initial sorption period (no light, no applied potential) and during the electrochemical (EC) transformation period (no light, +1.00 V *vs.* Ag/AgCl applied potential) for a CNF electrode (without $TiO_2$) and the optimal CNF/$TiO_2$ composite electrode (0.45 g PAN/50 wt% $TiO_2$/1000 °C). The pre-transformation sorption period was typically initiated 17 h prior to applying potential to the electrodes, as this timescale was sufficient to achieve sorption equilibrium. At the conclusion of the sorption period, controls revealed that all the CBZ bound to both electrodes could be recovered completely *via* extraction with either methanol or acetonitrile, confirming that no CBZ degradation occurred during this period. Although the initial CBZ concentration ($C_0$ = 10 μM) is greater than those typically encountered in environmental systems (μg $L^{-1}$ concentrations or less), current density during the transformation period was constant (see Fig. 6b), which indicates CBZ transformation was not concentration dependent (*i.e.*, not mass transfer limited). Thus, we would expect comparable performance at lower, more

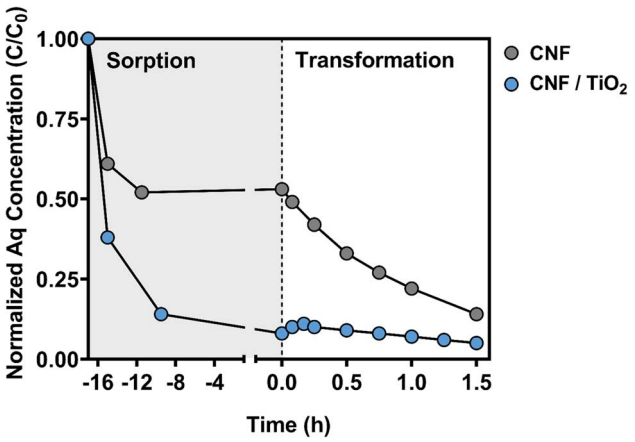


Fig. 5 Normalized aqueous (Aq) carbamazepine (CBZ) concentration ($C/C_0$; $C_0$ = 10 μM CBZ) over time during the sorption and electrochemical (EC) transformation periods. CBZ sorption was conducted in the dark, without an applied potential. The EC transformation was conducted at +1.00 V (*vs.* Ag/AgCl). Data are shown for the optimal composite (0.45 g PAN/50 wt% $TiO_2$/1000 °C) and for CNFs without $TiO_2$ carbonized at 1000 °C.

environmentally relevant concentrations, particularly given the excess of electrode surface area available for sorption and transformation.

In the CNF electrode system, ~50% of the available CBZ sorbed to the electrode over this initial sorption period (see Fig. 5). This degree of CBZ uptake is far greater than that observed in our previous study using similar composites for photocatalytic water treatment.[47] However, CNFs and their $TiO_2$ composites in our previous work were carbonized at a lower temperature (typically 450 °C), and thus would be expected to exhibit less graphitic character than the composites investigated herein. As CBZ is a moderately hydrophobic chemical (with a logarithmic octanol–water partition coefficient of 2.45),[78] the greater extent of CBZ sorption observed herein can likely be attributed to the greater hydrophobicity of CNFs generated at higher carbonization temperatures.

During the sorption period, CBZ uptake was faster and occurred to a far greater extent (~90%) on CNF/$TiO_2$ composites carbonized at 1000 °C relative to CNFs without $TiO_2$ (see Fig. 5). Additional studies with CNF/$TiO_2$ composites confirmed that the extent of CBZ sorption increased with carbonization

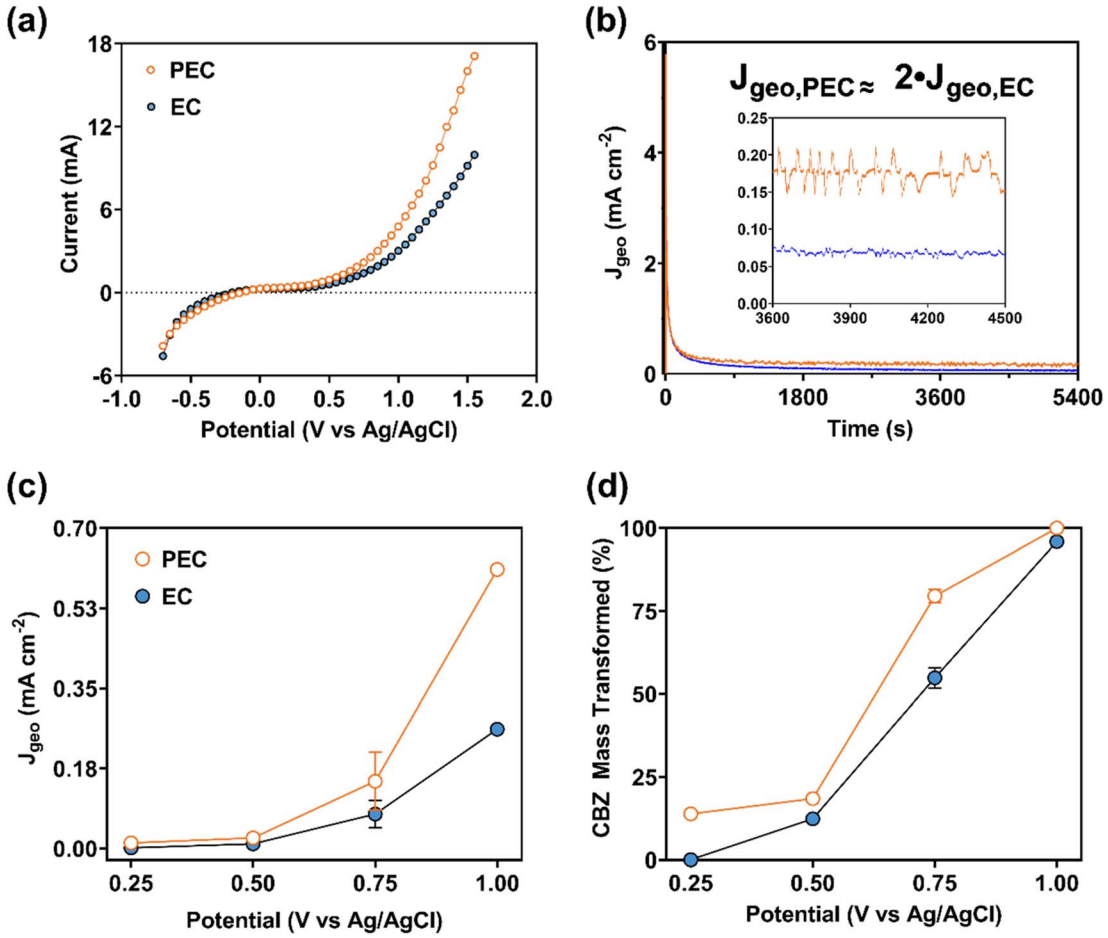


Fig. 6 For the optimal (0.45 g PAN/50 wt% $TiO_2$/1000 °C) CNF/$TiO_2$ composite: (a) average faradaic current resulting from staircase cyclic voltammetry (SCV; 50 mV, 30 s, −0.7 to 1.5 V) with and without light; (b) representative current density–time profiles for photoelectrochemical (PEC) and electrochemical (EC) transformation at +0.75 V *vs.* Ag/AgCl; (c) average faradaic current density during PEC and EC transformation (300–5400 s); and (d) CBZ mass transformed (%) during PEC and EC transformation (0–5400 s). Parameters: $C_0$ = 10 μM CBZ, 0.5 M phosphate buffer at pH 7.4.

temperature (Fig. S13†), consistent with expectations from the behavior of CNFs. Compared to the CNF electrode, the increased sorption capacity of the CNF/$TiO_2$ composites is notable because the surface hydroxyl groups of the oxide should produce a more polar surface that hinders hydrophobic partitioning of CBZ. It is likely that the increased CBZ uptake is due in part to the greater degree of surface area available on CNF/$TiO_2$ composites.[47] It is also possible that there are other, more specific binding interactions (*e.g.*, H-bonding, van der Waals forces) that are promoted by the surface hydroxyl groups on $TiO_2$ that can also contribute to CBZ uptake. Regardless, at the start of the transformation period, nearly all of the CBZ mass is bound to the electrode for CNF/$TiO_2$ composites, and only a small fraction ($C/C_0 < 0.1$) remains available in the aqueous phase.

During the EC transformation period, evidence suggests that degradation of both aqueous and sorbed CBZ occurs with CNF and CNF/$TiO_2$ electrodes. In the CNF system, which started with roughly equal portions of CBZ in the aqueous and sorbed phase, a near exponential decrease in aqueous CBZ was observed over time upon application of +1.00 V to the electrode. In contrast, slightly different behavior was observed for the aqueous phase concentration of CBZ in the CNF/$TiO_2$ composite system, where CBZ concentration initially, albeit briefly, increased before slowly decaying away over time. We attribute the slight increase to electrostatic repulsion from the positively charged electrode surface in response to the applied potential, which in turn promoted the release of the previously bound CBZ.

At the conclusion of the 90 minute EC transformation period, a small portion of CBZ was detected in methanol extracts of the CNF electrode, indicating that some CBZ remained bound to the electrode at the conclusion of the reaction (approximately 10% of the initial concentration). With roughly 15% of the initial CBZ concentration also remaining in the aqueous phase at the conclusion of the transformation period, evidence suggests that the remaining 75% of CBZ mass was degraded *via* electrochemical oxidation on the CNFs over the 90 minute period. For CNF/$TiO_2$ electrodes, CBZ was not detected in methanol extracts and only ~5% remained in aqueous solution, suggesting that there was near-complete degradation of CBZ using the CNF/$TiO_2$ composites. Thus, evidence suggests that CNF/$TiO_2$ composite electrodes were able to achieve a greater extent of CBZ electrochemical oxidation relative to unmodified CNFs over the same transformation period.

**Potential dependent (photo)electrochemical CBZ transformation on CNF/$TiO_2$.** Aqueous CBZ concentration profiles with the optimal CNF/$TiO_2$ electrode (0.45 g PAN/50 wt% $TiO_2$/1000 °C) are provided in Fig. S14† as a function of applied potential during the EC and PEC transformation periods (from +0.25 to +1.00 V). In all cases, sorption behavior followed expectations based on the results in Fig. 5, with ~90% CBZ uptake on the CNF/$TiO_2$ composite during the 17 h prior to the transformation period (data not shown).

During the EC transformation period, the aqueous CBZ concentration varied over time, as in Fig. 5, but its behavior depended on system conditions (*i.e.*, applied potential, light *versus* dark). More discussion is provided in the ESI,† but there were three general trends in aqueous CBZ over time in these systems: (i) at low applied potential, very low aqueous CBZ concentrations remained essentially constant over the transformation period; (ii) at intermediate applied potentials, aqueous CBZ increased over time consistent with release of sorbed CBZ from the electrode; and (iii) at higher potentials, aqueous CBZ often exhibited an initial, very brief increase before decreasing over time, consistent with degradation *via* electrochemical oxidation. Notably, aqueous CBZ transformation was more prominent in PEC systems, which exhibited decreases in aqueous concentration over time at lower applied potentials than in EC systems. For example, in PEC systems at +1.00 V, aqueous CBZ was not detected after the first 15 minutes of the transformation period; notably, aqueous CBZ was detectable over the entire EC transformation period at +1.00 V. With light only (no applied potential) for 90 minutes, no CBZ degradation (photolysis) was observed ($C/C_0 \approx 1.0$).

The electrochemical performance for the CNF/$TiO_2$ electrode during EC and PEC transformation is summarized in Fig. 6. Collectively, results in Fig. 6 are consistent with the (photo) electrochemical transformation of CBZ in both the EC and PEC systems. For example, SCV (Fig. 6a) clearly captured the faradaic current of the CNF/$TiO_2$ composites in the EC system with CBZ, also illustrating the relevant applied potential range where faradaic current increased when the composite was exposed to light in the PEC system. Faradaic current in the PEC system began to deviate from the current in the EC system at approximately +0.25 V; for example, at +1.55 V, the irradiated CNF/$TiO_2$ composite produced a current that was ~70% greater than in the dark EC system.

Greater activity in PEC systems relative to EC systems is also supported by measurements of the geometric current density ($J_{geo}$ *vs.* $t$), as shown in Fig. 6b for transformation experiments at +0.75 V. Higher current density was consistently observed in PEC systems relative to EC systems ($J_{geo,PEC} \approx 2J_{geo,EC}$), illustrating the ability of UV-light to enhance CBZ transformation at a given potential. PEC current density was greater than EC current density at several of the applied potentials investigated (+0.50, 0.75, and 1.00 V; see Fig. 6c), with the greatest difference observed at +1.00 V. Consistent with SCV results, a minimal difference in PEC and EC current was observed at +0.25 V.

Based on a mass balance of CBZ in experimental systems, we were able to calculate the amount of CBZ transformed (%) at the end of the 90 minute transformation period as a function of applied potential in EC and PEC systems (Fig. 6d). The extent of CBZ transformation increased with applied potential, and for a given potential PEC consistently transformed more total CBZ mass than EC, as anticipated from the greater current density in the PEC system (see Fig. 6c). Near complete CBZ transformation was observed at the conclusion of the 90 minute transformation period at +1.0 V in both EC and PEC systems, but it is likely that all of the CBZ in the PEC system was consumed prior to 90 minutes. Accordingly, we estimated the rate constant ($k_{obs}$) for the transformation of CBZ mass in EC and PEC systems at +1.0 V by quantifying the mass remaining in both the aqueous and sorbed phase after 15 minutes of reaction. As with other

advanced oxidation processes, the CBZ oxidation reaction was assumed as a pseudo-first-order process [*i.e.*, $\ln(C_t/C_0) = -k_{obs}t$],[79] allowing the determination of a single-point $k_{obs}$ value based on the change in total CBZ mass over this 15 minute interval. Based on these estimated $k_{obs}$ values at +1.00 V, the rate of CBZ transformation was roughly 1.5-fold faster in the PEC [$k_{obs}$(PEC) = 0.18 $min^{-1}$] system relative to the EC system [$k_{obs}$(EC) = 0.12 $min^{-1}$], corresponding to half-lives of 3.8 and 5.8 minutes, respectively. Applying this same approach to the CNF electrode in Fig. 5, we obtained a rate constant for total CBZ transformation of 0.015 $min^{-1}$ (corresponding to a half-life of roughly 45 minutes), which is roughly one order of magnitude less than the $k_{obs}$ values measured for CNF/$TiO_2$ composites.

The rate constants for CNF/$TiO_2$ composites in EC and PEC systems compare favorably to those previously reported for CBZ transformation with other advanced water treatment processes.[79] These rate constants also meet or surpass the rate constants for photocatalysis as obtained with metal-augmented carbon catalysts and electrospun $TiO_2$ fibers.[52,53] Moreover, these rate constants also meet or exceed those reported for EC oxidation as obtained at lower supporting electrolyte concentrations with commercial electrodes.[80,81] These comparison rates, and corresponding experimental parameters, are presented in Table S6.† Unlike the CNF/$TiO_2$ composites presented herein, other nanostructured $TiO_2$ electrodes exhibited little to no CBZ degradation for EC conditions (bias only) in the presence of real secondary effluent wastewater spiked with CBZ (10 μg $L^{-1}$).[82]

**Electrochemical stability testing of CNF/$TiO_2$ electrodes.** As a final performance test, we also considered the CNF/$TiO_2$ (0.45 g PAN/50 wt% $TiO_2$/1000 °C) electrode stability and reactivity across 5 reaction cycles with CBZ (*i.e.*, sorption and transformation) in the EC system at +1.00 V (Fig. 7). Notably, the aqueous CBZ concentration present at the start of the transformation period (after sorption) increased with each successive trial, suggesting that the sorption capacity of the CNF/$TiO_2$ electrode decreased with each cycle. While >90% of the initial 10 μM CBZ concentration was sorbed during the first cycle, CBZ uptake during the sorption period decreased to only ~30% by the fifth reaction cycle. We speculate that the decrease in electrode sorption capacity is most likely due to the accumulation of CBZ transformation products on the electrode surface because no measurable CBZ was detected in methanol extracts of the CNF electrode at the conclusion of the 5 cycles.

Despite the loss in sorption capacity, it does not appear that the electrochemical performance of the electrode was diminished over the five reaction cycles. In fact, measured current densities ($J_{geo}$) were almost constant across all trials, with an average value of 0.25 (±0.03) mA $cm^{-2}$ across the 5 cycles. The trends in aqueous CBZ concentration over time during the transformation period, particularly in later cycles, also suggest sustained electrode performance. In the first two cycles, CBZ was released from the surface upon the application of +1.00 V, as was observed in Fig. 5 and S14† for EC systems and suggesting that most of the CBZ transformation during these cycles resulted from oxidation of CBZ previously sorbed to the electrode surface. In later cycles (three through five), however, when electrode sorption capacity decreased, the near-equivalent rate of aqueous CBZ decay over time (corresponding to a $k_{obs}$ of ~0.008 $min^{-1}$ in each cycle, assuming exponential decay), suggests a comparable transformation of CBZ for these systems.

Based on the results of these cycling experiments, we conceptualize the CNF/$TiO_2$ composite electrodes as having at least two distinct surface sites. One surface site (or family of sites) is primarily responsible for sorption of CBZ, and likely consists primarily of the graphitic carbon generated during carbonization. A second surface site (or family of sites) appears primarily responsible for charge transfer, and these presumably consist of the embedded $TiO_2$ surfaces. We propose distinct

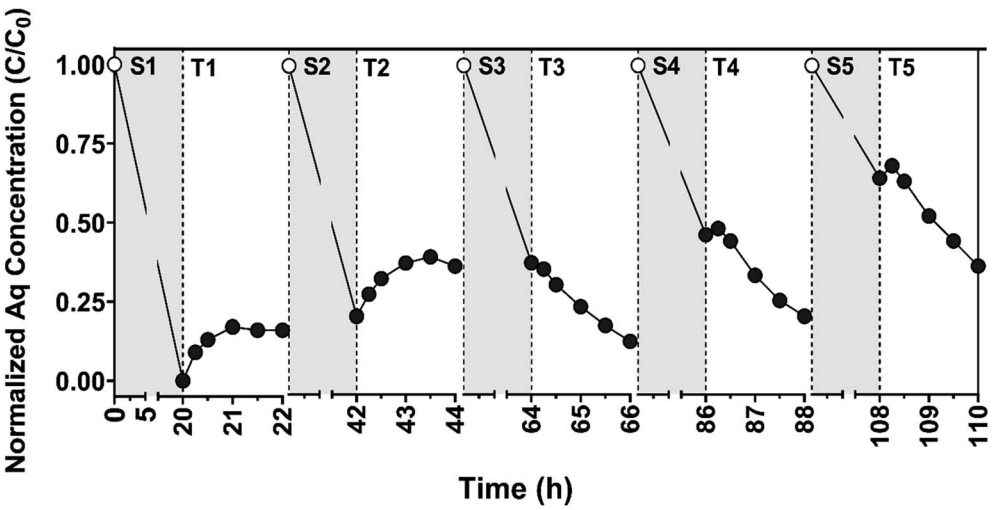


Fig. 7 Normalized aqueous (Aq) CBZ concentration ($C/C_0$; $C_0$ = 10 μM CBZ) observed during the sorption (gray) and transformation (white) periods during cycling experiments to test the long-term stability and reactivity of CNF/$TiO_2$ composites (0.45 g PAN/50 wt% $TiO_2$/1000 °C) across five cycles. Electrochemical (EC) transformation occurred at +1.0 V *vs.* Ag/AgCl. Lines do not represent model fits and are only shown to help illustrate trends in data.

sites for sorption and charge transfer because sorption capacity markedly decreased across the five reaction cycles while current density, a measure of charge transfer, was effectively unchanged. Because the majority of CBZ in the system is sorbed to the electrode during early transformation cycles, surface-bound CBZ must be loosely held and able to migrate between sorption and charge transfer sites to allow for the extent of transformation that we observed. Accordingly, and because CBZ was not detected in extracts of the electrode at the conclusion of the five reaction cycles, we speculate that some CBZ transformation products must be more irreversibly bound to sorption sites such that they are occupied and no longer available for CBZ uptake. We emphasize that the loss of sorption capacity does not appear to be detrimental to electrode performance during applications in water treatment; in the later cycles, based off the decay in CBZ concentration over time in aqueous solution, the electrode continued to achieve rate constants for CBZ degradation that are comparable to those reported for some UV-based treatment of CBZ.[79]

## Conclusion

Herein, we demonstrate that electrospun CNF/$TiO_2$ composites, when optimized for their physical and (photo)chemical properties, can function as promising (photo)electrodes for advanced water treatment applications. Electrospinning provides a reproducible, single-batch synthesis approach for producing electroactive nanomaterial composites with tunable performance properties. Using this synthesis approach, we were able to enhance the performance of standard CNFs by easily integrating photoactivity (through the addition of $TiO_2$ nanoparticles) and tailoring conductivity (through carbonization temperature) without need for more extensive material post-processing or surface modification (*e.g.*, doping, etching, physical vapor deposition). CNF/$TiO_2$ composites produced *via* electrospinning hold the advantages of easily controlled $TiO_2$ loading, bulk chemical structure, and diffusivity (which is important for applications targeting contaminants at low environmental concentrations), while also being able to maintain high surface area and mechanical integrity after heat treatment. Detailed structural and electrochemical characterizations found that the optimized CNF/$TiO_2$ (photo)electrodes exhibited high surface area (50 $m^2$ $g^{-1}$) and low geometric (areal) resistance (2.66 Ω $cm^2$). Notably, we also demonstrate that these CNF/$TiO_2$ composites can be successfully applied as a free-standing, binder-free electrode to transform a recalcitrant water contaminant (CBZ), which may enable the use of such systems for renewably driven water treatment. Indeed, a benefit of this composite electrode material is its ability to outperform more traditional CNF electrodes when used in either electrochemical or photoelectrochemical treatment configurations.

There are several other practical advantages of these composite (photo)electrodes relative to other commercially available electrodes and electrode synthesis approaches. In producing these materials, we avoided the use of expensive, unsustainable, and/or rare materials, such as noble metals that are commonly integrated *via* nanoparticles, coatings, or thin films to augment electrode performance. Our electrodes add to the existing body of research demonstrating that nanoparticles (*e.g.*, $TiO_2$) commonly used in dispersions that are difficult to apply at water treatment scale can maintain performance in EC and PEC systems when immobilized into conductive platforms. Further, as with commercial carbon electrodes, the CNF (photo) electrode material can be fabricated with sufficient strength to withstand routine handling (*e.g.*, bend, twist; see Fig. S9†) and versatile deployment across a range of reactor configurations.

There remain several opportunities to further validate and improve upon the performance of electrode materials. From the material performance demonstrated here, an EC or PEC system equipped with the CNF (photo)electrodes would be well-suited as a final polishing step for drinking water to remove micropollutant mixtures, where competition and fouling from other dissolved co-solutes would be minimal. Moreover, electrode performance can likely be improved further if used as an electroactive membrane in a flow-through system designed to alleviate mass transfer limitations; our previous efforts with the photoactive CNF/$TiO_2$ composites demonstrated the ability to remove the majority of recalcitrant organic micropollutants in a single pass during dead end filtration at fluxes comparable to that required for microfiltration (540 L $m^{-2}$ $h^{-1}$).[47] While promising, better removals efficiencies toward a wider range of contaminants should be achievable using an analogous photoelectroactive membrane. Therefore, future work will need to assess the performance of CNF/$TiO_2$ composites in reactive filtration systems at comparable fluxes under EC and PEC conditions and toward a broader suite of recalcitrant organic micropollutants. Using such a configuration, it may also be possible to alleviate the loss of electrode sorption capacity over time (see Fig. 7) through periodic regeneration or washing steps (*e.g.*, with acid, base or an organic solvent).

## Conflicts of interest

There are no conflicts to declare.

## References

1 J. Radjenovic and D. L. Sedlak, Challenges and Opportunities for Electrochemical Processes as Next-Generation Technologies for the Treatment of Contaminated Water, *Environ. Sci. Technol.*, 2015, **49**, 11292–11302.
2 B. P. Chaplin, The Prospect of Electrochemical Technologies Advancing Worldwide Water Treatment, *Acc. Chem. Res.*, 2019, **52**, 596–604.
3 S. Garcia-Segura, X. Qu, P. J. J. Alvarez, B. P. Chaplin, W. Chen, J. C. Crittenden, Y. Feng, G. Gao, Z. He, C.-H. Hou, X. Hu, G. Jiang, J.-H. Kim, J. Li, Q. Li, J. Ma, J. Ma, A. B. Nienhauser, J. Niu, B. Pan, X. Quan, F. Ronzani, D. Villagran, T. D. Waite, W. S. Walker, C. Wang, M. S. Wong and P. Westerhoff, Opportunities for nanotechnology to enhance electrochemical treatment of pollutants in potable water and industrial wastewater – a perspective, *Environ. Sci.: Nano*, 2020, **7**, 2178–2194.

4 N. Singh and B. R. Goldsmith, Role of Electrocatalysis in the Remediation of Water Pollutants, *ACS Catal.*, 2020, **10**, 3365–3371.
5 C. A. Martínez-Huitle and M. Panizza, Electrochemical oxidation of organic pollutants for wastewater treatment, *Curr. Opin. Electrochem.*, 2018, **11**, 62–71.
6 C. A. Martínez-Huitle and E. Brillas, Decontamination of wastewaters containing synthetic organic dyes by electrochemical methods: A general review, *Appl. Catal., B*, 2009, **87**, 105–145.
7 Z. Zheng and I. M. C. Lo, Multifunctional photoelectrochemical systems for coupled water treatment and high-value product generation: current status, mechanisms, remaining challenges, and future opportunities, *Curr. Opin. Electrochem.*, 2021, **34**, 100711.
8 S. Chang, Q. Wang, B. Liu, Y. Sang and H. Liu, Hierarchical TiO2 nanonetwork–porous Ti 3D hybrid photocatalysts for continuous-flow photoelectrodegradation of organic pollutants, *Catal. Sci. Technol.*, 2017, **7**, 524–532.
9 R. Song, H. Chi, Q. Ma, D. Li, X. Wang, W. Gao, H. Wang, X. Wang, Z. Li and C. Li, Highly Efficient Degradation of Persistent Pollutants with 3D Nanocone TiO2-Based Photoelectrocatalysis, *J. Am. Chem. Soc.*, 2021, **143**, 13664–13674.
10 S. Xiang, Z. Zhang, Z. Wu, L. Sun, P. Radjenovic, H. Ren, C. Lin, Z. Tian and J. Li, 3D Heterostructured Ti-Based Bi2MoO6/Pd/TiO2 Photocatalysts for High-Efficiency Solar Light Driven Photoelectrocatalytic Hydrogen Generation, *ACS Appl. Energy Mater.*, 2019, **2**, 558–568.
11 G. Wang, X. Xiao, W. Li, Z. Lin, Z. Zhao, C. Chen, C. Wang, Y. Li, X. Huang, L. Miao, C. Jiang, Y. Huang and X. Duan, Significantly Enhanced Visible Light Photoelectrochemical Activity in TiO2 Nanowire Arrays by Nitrogen Implantation, *Nano Lett.*, 2015, **15**, 4692–4698.
12 M. S. Koo, K. Cho, J. Yoon and W. Choi, Photoelectrochemical Degradation of Organic Compounds Coupled with Molecular Hydrogen Generation Using Electrochromic TiO2 Nanotube Arrays, *Environ. Sci. Technol.*, 2017, **51**, 6590–6598.
13 G. M. Peleyeju, E. H. Umukoro, J. O. Babalola and O. A. Arotiba, Solar-Light-Responsive Titanium-Sheet-Based Carbon Nanoparticles/B-BiVO4/WO3 Photoanode for the Photoelectrocatalytic Degradation of Orange II Dye Water Pollutant, *ACS Omega*, 2020, **5**, 4743–4750.
14 C. Liu, A.-Y. Zhang, Y. Si, D.-N. Pei and H.-Q. Yu, Photochemical Protection of Reactive Sites on Defective TiO2–x Surface for Electrochemical Water Treatment, *Environ. Sci. Technol.*, 2019, **53**, 7641–7652.
15 L. Barrera and R. Bala Chandran, Harnessing Photoelectrochemistry for Wastewater Nitrate Treatment Coupled with Resource Recovery, *ACS Sustainable Chem. Eng.*, 2021, **9**, 3688–3701.
16 J.-S. Yang, W. W.-P. Lai, S. C. Panchangam and A. Y.-C. Lin, Photoelectrochemical degradation of perfluorooctanoic acid (PFOA) with GOP25/FTO anodes: Intermediates and reaction pathways, *J. Hazard. Mater.*, 2020, **391**, 122247.
17 C. Wang, M. Sun, Y. Zhao, M. Huo, X. Wang and M. Elimelech, Photo-electrochemical Osmotic System Enables Simultaneous Metal Recovery and Electricity Generation from Wastewater, *Environ. Sci. Technol.*, 2021, **55**, 604–613.
18 D.-H. Nam, D. Lee and K.-S. Choi, Electrochemical and photoelectrochemical approaches for the selective removal, recovery, and valorization of chloride ions, *Chem. Eng. J.*, 2021, **404**, 126378.
19 K. Kinoshita and S. C. Leach, Mass-Transfer Study of Carbon Felt, Flow-Through Electrode, *J. Electrochem. Soc.*, 1993, **129**, 6.
20 X. You, Q. Ye and P. Cheng, The Dependence of Mass Transfer Coefficient on the Electrolyte Velocity in Carbon Felt Electrodes: Determination and Validation, *J. Electrochem. Soc.*, 2017, **164**, E3386–E3394.
21 B. P. Chaplin, Critical review of electrochemical advanced oxidation processes for water treatment applications, *Environ. Sci.: Processes Impacts*, 2014, **16**, 1182–1203.
22 R. McCreery, Advanced Carbon Electrode Materials for Molecular Electrochemistry, *Chem. Rev.*, 2008, **108**, 41.
23 X. Chen, G. Chen and P. L. Yue, Anodic oxidation of dyes at novel Ti/B-diamond electrodes, *Chem. Eng. Sci.*, 2003, **58**, 995–1001.
24 M. Qiao, Y. Zhang, L. Zhai and M. Sun, Corrosion of graphite electrode in electrochemical advanced oxidation processes: Degradation protocol and environmental implication, *Chem. Eng. J.*, 2018, **344**, 8.
25 M. Sun, X. Wang, L. R. Winter, Y. Zhao, W. Ma, T. Hedtke, J.-H. Kim and M. Elimelech, Electrified Membranes for Water Treatment Applications, *ACS ES&T Engg*, 2021, **1**, 725–752.
26 X. Zhu and D. Jassby, Electroactive Membranes for Water Treatment: Enhanced Treatment Functionalities, Energy Considerations, and Future Challenges, *Acc. Chem. Res.*, 2019, **52**, 1177–1186.
27 M. Shestakova and M. Sillanpää, Electrode materials used for electrochemical oxidation of organic compounds in wastewater, *Rev. Environ. Sci. Bio/Technol.*, 2017, **16**, 223–238.
28 M. J. Nalbandian, S. Kim, H. E. Gonzalez-Ribot, N. V. Myung and D. M. Cwiertny, Recent advances and remaining barriers to the development of electrospun nanofiber and nanofiber composites for point-of-use and point-of-entry water treatment systems, *J. Hazard. Mater. Adv.*, 2022, **8**, 100204.
29 W. Wu, Z.-H. Huang and T.-T. Lim, Recent development of mixed metal oxide anodes for electrochemical oxidation of organic pollutants in water, *Appl. Catal., A*, 2014, **480**, 58–78.
30 H. Wu, H. L. Tan, C. Y. Toe, J. Scott, L. Wang, R. Amal and Y. H. Ng, Photocatalytic and Photoelectrochemical Systems: Similarities and Differences, *Adv. Mater.*, 2020, **32**, 1904717.
31 Y. Han, S. Zhang, H. Zhao, W. Wen, H. Zhang, H. Wang and F. Peng, Photoelectrochemical Characterization of a Robust TiO2/BDD Heterojunction Electrode for Sensing Application in Aqueous Solutions, *Langmuir*, 2010, **26**, 6033–6040.
32 Y. Wang, M. Zu, X. Zhou, H. Lin, F. Peng and S. Zhang, Designing efficient TiO2-based photoelectrocatalysis

systems for chemical engineering and sensing, *Chem. Eng. J.*, 2020, **381**, 122605.
33 Y.-n. Zhang, Q. Niu, X. Gu, N. Yang and G. Zhao, Recent progress on carbon nanomaterials for the electrochemical detection and removal of environmental pollutants, *Nanoscale*, 2019, **11**, 11992–12014.
34 W. Zhang, S. Zhu, R. Luque, S. Han, L. Hu and G. Xu, Recent development of carbon electrode materials and their bioanalytical and environmental applications, *Chem. Soc. Rev.*, 2016, **45**, 715–752.
35 S. Peng, L. Li, J. Kong Yoong Lee, L. Tian, M. Srinivasan, S. Adams and S. Ramakrishna, Electrospun carbon nanofibers and their hybrid composites as advanced materials for energy conversion and storage, *Nano Energy*, 2016, **22**, 361–395.
36 L.-F. Chen, Y. Feng, H.-W. Liang, Z.-Y. Wu and S.-H. Yu, Macroscopic-Scale Three-Dimensional Carbon Nanofiber Architectures for Electrochemical Energy Storage Devices, *Adv. Energy Mater.*, 2017, **7**, 1700826.
37 R. Stirling, W. S. Walker, P. Westerhoff and S. Garcia-Segura, Techno-economic analysis to identify key innovations required for electrochemical oxidation as point-of-use treatment systems, *Electrochim. Acta*, 2020, **338**, 135874.
38 G. Song, M. Zhou, X. Du, P. Su and J. Guo, Mechanistic Insight into the Heterogeneous Electro-Fenton/Sulfite Process for Ultraefficient Degradation of Pollutants over a Wide pH Range, *ACS ES&T Water*, 2021, **1**, 1637–1647.
39 K. Deng, Y. Gu, T. Gao, Z. Liao, Y. Feng, S. Zhou, Q. Fang, C. Hu and L. Lyu, Carbonized MOF-Coated Zero-Valent Cu Driving an Efficient Dual-Reaction-Center Fenton-like Water Treatment Process through Utilizing Pollutants and Natural Dissolved Oxygen, *ACS ES&T Water*, 2022, **2**, 174–183.
40 S. O. Ganiyu, M. Zhou and C. A. Martínez-Huitle, Heterogeneous electro-Fenton and photoelectro-Fenton processes: A critical review of fundamental principles and application for water/wastewater treatment, *Appl. Catal., B*, 2018, **235**, 103–129.
41 S. K. Loeb, P. J. J. Alvarez, J. A. Brame, E. L. Cates, W. Choi, J. Crittenden, D. D. Dionysiou, Q. Li, G. Li-Puma, X. Quan, D. L. Sedlak, T. David Waite, P. Westerhoff and J. H. Kim, The Technology Horizon for Photocatalytic Water Treatment: Sunrise or Sunset?, *Environ. Sci. Technol.*, 2019, **53**, 2937–2947.
42 M. A. Lazar, S. Varghese and S. S. Nair, Photocatalytic Water Treatment by Titanium Dioxide: Recent Updates, *Catalysts*, 2012, **2**, 572–601.
43 S. Franz, E. Falletta, H. Arab, S. Murgolo, M. Bestetti and G. Mascolo, Degradation of Carbamazepine by Photo(electro)catalysis on Nanostructured TiO2 Meshes: Transformation Products and Reaction Pathways, *Catalysts*, 2020, **10**, 169.
44 J. Matos, S. Miralles-Cuevas, A. Ruíz-Delgado, I. Oller and S. Malato, Development of TiO2-C photocatalysts for solar treatment of polluted water, *Carbon*, 2017, **122**, 361–373.
45 P. Aghasiloo, M. Yousefzadeh, M. Latifi and R. Jose, Highly porous TiO2 nanofibers by humid-electrospinning with enhanced photocatalytic properties, *J. Alloys Compd.*, 2019, **790**, 257–265.
46 S. Kim, G. Piao, D. S. Han, H. K. Shon and H. Park, Solar desalination coupled with water remediation and molecular hydrogen production: a novel solar water-energy nexus, *Energy Environ. Sci.*, 2018, **11**, 344–353.
47 K. E. Greenstein, M. R. Nagorzanski, B. Kelsay, E. M. Verdugo, N. V. Myung, G. F. Parkin and D. M. Cwiertny, Carbon–titanium dioxide (C/TiO2) nanofiber composites for chemical oxidation of emerging organic contaminants in reactive filtration applications, *Environ. Sci.: Nano*, 2021, **8**, 711–722.
48 R. Montenegro-Ayo, J. C. Morales-Gomero, H. Alarcon, A. Corzo, P. Westerhoff and S. Garcia-Segura, Photoelectrocatalytic degradation of 2,4-dichlorophenol in a TiO2 nanotube-coated disc flow reactor, *Chemosphere*, 2021, **268**, 129320.
49 B. Zhang, F. Yang, H. Liu, L. Yan, W. Yang, C. Xu, S. Huang, Q. Li, W. Bao, B. Liu and Y. Li, Assembling Graphene-Encapsulated Pd/TiO2 Nanosphere with Hierarchical Architecture for High-Performance Visible-Light-Assisted Methanol Electro-Oxidation Material, *Ind. Eng. Chem. Res.*, 2019, **58**, 19486–19494.
50 L. Persano, A. Camposeo, C. Tekmen and D. Pisignano, Industrial Upscaling of Electrospinning and Applications of Polymer Nanofibers: A Review, *Macromol. Mater. Eng.*, 2013, **298**, 504–520.
51 T. Kosjek, H. R. Andersen, B. Kompare, A. Ledin and E. Heath, Fate of Carbamazepine during Water Treatment, *Environ. Sci. Technol.*, 2009, **43**, 6.
52 G. Chen, W. Dong, H. Wang, Z. Zhao, F. Wang, F. Wang and C. Nieto-Delgado, Carbamazepine degradation by visible-light-driven photocatalyst Ag3PO4/GO: Mechanism and pathway, *Environ. Sci. Ecotechnology*, 2022, **9**, 100143.
53 S. K. Maeng, K. Cho, B. Jeong, J. Lee, Y. Lee, C. Lee, K. J. Choi and S. W. Hong, Substrate-immobilized electrospun TiO2 nanofibers for photocatalytic degradation of pharmaceuticals: The effects of pH and dissolved organic matter characteristics, *Water Res.*, 2015, **86**, 25–34.
54 K. T. Peter, J. D. Vargo, T. P. Rupasinghe, A. De Jesus, A. V. Tivanski, E. A. Sander, N. V. Myung and D. M. Cwiertny, Synthesis, Optimization, and Performance Demonstration of Electrospun Carbon Nanofiber-Carbon Nanotube Composite Sorbents for Point-of-Use Water Treatment, *ACS Appl. Mater. Interfaces*, 2016, **8**, 11431–11440.
55 Y. Zhang, N. Tajaddod, K. Song and M. L. Minus, Low temperature graphitization of interphase polyacrylonitrile (PAN), *Carbon*, 2015, **91**, 479–493.
56 M. Inagaki, Y. Yang and F. Kang, Carbon nanofibers prepared via electrospinning, *Adv. Mater.*, 2012, **24**, 2547–2566.
57 M. S. A. Rahaman, A. F. Ismail and A. Mustafa, A review of heat treatment on polyacrylonitrile fiber, *Polym. Degrad. Stab.*, 2007, **92**, 1421–1432.
58 D. Edie, The effect of processing on the structure and properties of carbon fibers, *Carbon*, 1998, **36**, 18.

59 N. Yusof and A. F. Ismail, Post spinning and pyrolysis of processes of polyacrylonitrile (PAN)-based carbon fiber and activated carbon fiber: A review, *J. Anal. Appl. Pyrolysis*, 2012, **93**, 13.

60 F. Tuinstra and J. L. Koenig, Raman Spectrum of Graphite, *J. Chem. Phys.*, 1970, **53**, 1126–1130.

61 M. A. Pimenta, G. Dresselhaus, M. S. Dresselhaus, L. G. Cancado, A. Jorio and R. Saito, Studying disorder in graphite-based systems by Raman spectroscopy, *Phys. Chem. Chem. Phys.*, 2007, **9**, 1276–1291.

62 Standard Test Method for Tensile Properties of Thin Plastic Sheeting ASTM International, 2018, ASTM D882-18.

63 T. Q. Nguyen and C. Breitkopf, Determination of Diffusion Coefficients Using Impedance Spectroscopy Data, *J. Electrochem. Soc.*, 2018, **165**, E826–E831.

64 J. M. Deitzel, J. Kleinmeyer, D. Harris and N. C. Beck Tan, The effect of processing variables on the morphology of electrospun nanofibers and textiles, *Polymer*, 2001, **42**, 261–272.

65 B. Zhang, F. Kang, J.-M. Tarascon and J.-K. Kim, Recent advances in electrospun carbon nanofibers and their application in electrochemical energy storage, *Prog. Mater. Sci.*, 2016, **76**, 319–380.

66 H. Kakida and K. Tashiro, Mechanism and Kinetics of Stabilization Reaction of Polyacrylonitrile and Related Copolymers II. Relationships between Iosthermal DSC Thermograms and FT-IR Spectral Changes of Polyacrylonitrile in Comparison with the Case of Acrylonitrile/Methacrylic Acid Copolymer, *Polym. J.*, 1997, **29**, 5.

67 A. Oberlin, Carbonization and Graphitization, *Carbon*, 1984, **22**, 21.

68 Phthalic acid and its isomers (isophthalic acid and terephthalic acid) [MAK Value Documentation, 2009], in *The MAK-Collection for Occupational Health and Safety*, 2012, DOI: 10.1002/3527600418.mb8899isme0025.

69 B. I. Waisi, S. S. Manickam, N. E. Benes, A. Nijmeijer and J. R. McCutcheon, Activated Carbon Nanofiber Nonwovens: Improving Strength and Surface Area by Tuning Fabrication Procedure, *Ind. Eng. Chem. Res.*, 2019, **58**, 4084–4089.

70 E. Frank, L. M. Steudle, D. Ingildeev, J. M. Spörl and M. R. Buchmeiser, Carbon Fibers: Precursor Systems, Processing, Structure, and Properties, *Angew. Chem., Int. Ed.*, 2014, **53**, 5262–5298.

71 R. I. Bickley, T. Gonzalez-Carreno, T. S. Lees, L. Palmisano and R. J. Tilley, Structural Investigation of Titanium Dioxide Photocatalysts, *J. Solid State Chem.*, 1991, **92**, 178–190.

72 G. Cerrato, L. Marchese and C. Morterra, Structural and morphological modifications of sintering microcrystalline TiO2: an XRD, HRTEM and FTIR study, *Appl. Surf. Sci.*, 1993, **70/71**, 200–205.

73 A. Elmouwahidi, E. Bailón-García, J. Castelo-Quibén, A. F. Pérez-Cadenas, F. J. Maldonado-Hódar and F. Carrasco-Marín, Carbon–TiO2 composites as high-performance supercapacitor electrodes: synergistic effect between carbon and metal oxide phases, *J. Mater. Chem. A*, 2018, **6**, 633–644.

74 H. Lu, C. Yang, H. Bao, L. Wang, C. Li and H. Wang, Unusual Improvement of Pseudocapacitance of Nanocomposite Electrodes: Three-Dimensional Amorphous Carbon Frameworks Triggered by TiO2 Nanocrystals, *ACS Appl. Mater. Interfaces*, 2019, **11**, 48039–48053.

75 H. Lin, X. Ji, Q. Chen, Y. Zhou, C. E. Banks and K. Wu, Mesoporous-TiO2 nanoparticles based carbon paste electrodes exhibit enhanced electrochemical sensitivity for phenols, *Electrochem. Commun.*, 2009, **11**, 1990–1995.

76 L.-C. Jiang and W.-D. Zhang, Electrodeposition of TiO2 Nanoparticles on Multiwalled Carbon Nanotube Arrays for Hydrogen Peroxide Sensing, *Electroanalysis*, 2009, **21**, 988–993.

77 A. Ramadoss and S. J. Kim, Improved activity of a graphene–TiO2 hybrid electrode in an electrochemical supercapacitor, *Carbon*, 2013, **63**, 434–445.

78 P. Westerhoff, Y. Yoon, S. Snyder and E. Wert, Fate of Endocrine-Disruptor, Pharmaceutical, and Personal Care Product Chemicals during Simulated Drinking Water Treatment Processes, *Environ. Sci. Technol.*, 2005, **39**, 6649–6663.

79 C.-m. Dai, X.-f. Zhou, Y.-l. Zhang, Y.-p. Duan, Z.-m. Qiang and T. C. Zhang, Comparative study of the degradation of carbamazepine in water by advanced oxidation processes, *Environ. Technol.*, 2012, **33**, 1101–1109.

80 J. D. García-Espinoza, P. Mijaylova-Nacheva and M. Avilés-Flores, Electrochemical carbamazepine degradation: Effect of the generated active chlorine, transformation pathways and toxicity, *Chemosphere*, 2018, **192**, 142–151.

81 C. García-Gómez, P. Drogui, F. Zaviska, B. Seyhi, P. Gortáres-Moroyoqui, G. Buelna, C. Neira-Sáenz, M. Estrada-alvarado and R. G. Ulloa-Mercado, Experimental design methodology applied to electrochemical oxidation of carbamazepine using Ti/PbO2 and Ti/BDD electrodes, *J. Electroanal. Chem.*, 2014, **732**, 1–10.

82 S. Murgolo, S. Franz, H. Arab, M. Bestetti, E. Falletta and G. Mascolo, Degradation of emerging organic pollutants in wastewater effluents by electrochemical photocatalysis on nanostructured TiO2 meshes, *Water Res.*, 2019, **164**, 114920.